Investigation of drying-induced non-uniform deformation, stress, and micro-crack propagation in concrete

Gao, Peng; Chen, Yang; Huang, Haoliang; Qian, Zhiwei; Schlangen, Erik; Wei, Jiangxiong; Yu, Qijun

Investigation of drying-induced non-uniform deformation, stress, and micro-crack propagation in concrete

Peng Gao [a], Yang Chen [a,c], Haoliang Huang [a,b], Zhiwei Qian [d], Erik Schlangen [e], Jiangxiong Wei [a,b,*], Qijun Yu [a,b]

[a] School of Materials Science and Engineering, South China University of Technology, Guangzhou, 510640, China
[b] Guangdong Low Carbon Technologies Engineering Centre for Building Materials, Guangzhou, 510640, China
[c] Guangdong Provincial Academy of Building Research Group Co., Ltd., Guangzhou, 510500, China
[d] FEMRIS, The Hague, CJ, 2497, the Netherlands
[e] Microlab, Faculty of Civil Engineering and Geosciences, Delft University of Technology, Delft, CN, 2628, the Netherlands

ARTICLE INFO

ABSTRACT

Concrete generally deforms and cracks in a non-uniform manner under drying-induced stress. This study used the lattice fracture model to simulate the drying-induced non-uniform deformations, stresses, and micro-crack propagation in concrete. Experiments were designed to validate the lattice fracture model, wherein the drying-induced non-uniform deformations and micro-crack patterns in concrete were measured using a digital image correlation technique and a fluorescent epoxy impregnation method, respectively. It was found that the simulated non-uniform deformations and micro-crack patterns were close to the experimental observations. The interaction mechanism between drying-induced non-uniform stresses and micro-cracks was analysed based on the validated lattice fracture model. The micro-cracks were found to cause stress concentration both in coarse aggregate and the mortar that covered coarse aggregate, which could lead to high micro-cracking risk as drying continues.

1. Introduction

Drying-induced shrinkage in concrete could cause serious deterioration of concrete structures [1–3]. As heterogeneous materials, concrete generally deforms in a non-uniform manner under drying stresses [4–6]. Hence, to evaluate the influence of drying-induced shrinkage on the performance of concrete, it is important to capture the local non-uniform deformations, stresses, and micro-cracks.

Computer technology models mainly simulate the drying-induced shrinkage of concrete using structure-based approaches, because such approaches cannot only be used to predict the bulk shrinkage of concrete, but also have advantages with regard to simulating local non-uniform deformations and micro-cracks [7–18]. Amongst them, the lattice fracture model has generated considerable interest in recent years [9,14–18]. In classical finite element model (FEM) the structure of materials is represented as continuum (solid) elements, while in the lattice fracture model the structure of materials is discretised into a network of lattice elements [19]. Moreover, a sequence of linear analysis is used in the lattice fracture model to simulate the non-linear

behaviours of materials [9,19], and shows high efficiency to deal with the non-uniform behaviours of concrete in terms of computer memory and computing time. By using the lattice fracture model, Grassl et al. [9] investigated the influence of aggregate size and volume on the drying-induced shrinkage and micro-cracks in the concrete embedded with spherical aggregates. Schlangen et al. [14,15] transformed the image of concrete into a lattice representation, and simulated the autogenous shrinkage of concrete using the lattice fracture model, wherein the autogenous shrinkage of cement paste was loaded onto the concrete lattice representation. Luković et al. [16] used a spatial aggregate packing model, namely, the Anm model [20], to establish the meso-structure of concrete, and coupled the lattice moisture model with the lattice fracture model to simulate the drying-induced moisture distribution, deformations, and cracks in concrete repair systems. Lin et al. [17,18] also used the lattice fracture model to simulate the drying shrinkage of cement paste, mortar, and concrete at different scales, respectively.

However, the simulation results of structure-based models are affected by many factors such as mesh generation and boundary

---

conditions. In different studies the simulation results of structure-based models might be different or even controversial. For example, in the simulation of Grassl et al. [9] the density of micro-cracks was found to decrease with increasing aggregate size, while in the simulation of Idiart et al. [11] the density of micro-cracks was found to increase with increasing aggregate size. Hence, it is necessary to carry out model validation. In the validation of structure-based models, bulk volume or linear drying shrinkage are frequently used [17,18], because the bulk drying shrinkage are easy to be determined. However, local information, and particularly local non-uniform deformations, simulated with these models have rarely been compared through experiments because the measurement of local non-uniform deformations is a challenging task.

In recent decades, digital image approaches are attracting increasing interest for measuring the local non-uniform deformations in cement-based materials. For example, the digital image correlation (DIC) technique is increasingly used for measuring the local non-uniform deformations of mortar [21] and concrete [6,22–26]. The DIC technique compares the digital images of specimens captured before and after the deformations. This technique has two variations: 2D-DIC, which requires one camera to measure two-dimensional deformations; 3D-DIC, which requires two cameras to measure three-dimensional deformations. Notably, Maruyama and Sasano [6] measured the local drying-induced non-uniform deformations and micro-cracks in concrete structures using the 2D-DIC technique and a fluorescent epoxy impregnation method, respectively, and confirmed the correlation between local micro-cracks and the macroscopic strain of concrete. Moreover, they [27] used a finite-element-based model (rigid-body-spring networks) to simulate the drying-induced crack propagation in concrete. However, the simulation of drying-induced deformations was not quantitatively compared with the DIC measurement in their reports [27]. In a previous study by our group, the 3D-DIC technique was used to investigate the influence of aggregate size and volume on the local drying-induced non-uniform deformations of concrete [26]. With the development of digital image approaches, it has become obvious that such approaches can provide sufficient non-uniform deformation data to validate structure-based models.

In this study, the lattice fracture model was used to simulate the local drying-induced non-uniform deformations, stresses, and micro-crack propagation in concrete. To validate the lattice fracture model using the experimental data, the local drying-induced non-uniform deformations and micro-cracks were measured using the 3D-DIC technique and the fluorescent epoxy impregnation method, respectively. Another objective of this study was to clarify the interaction between drying-induced micro-crack propagation and non-uniform stresses in concrete by using the validated lattice fracture model. Generally, the development of drying-induced micro-cracks in concrete is directly correlated with the non-uniform stresses [6,28,29]. With ongoing drying, the drying shrinkage force changes the non-uniform stresses in concrete. In addition, the formation of micro-cracks might redistribute the non-uniform stresses, which could affect the formation of new micro-cracks in further drying process. Since the non-uniform stresses in concrete are also influenced by the properties of concrete components, such as the size, volume, and shape of aggregates, the interaction between drying-induced micro-crack propagation and non-uniform stresses in concrete could be significant in the mix design of concrete. However, this interaction mechanism remains unclear in literature.

2. Experiments

2.1. Materials and mix proportions

C40 concrete was designed and its mix proportion was shown in Table 1. The Type I 42.5 cement was used as binder, the manufactured sand with a fineness modulus of 2.8 was used as fine aggregate, and the crushed granite (5–10 mm and 16–20 mm) was used as coarse aggregate. The volume fraction of total aggregates was 60%, and the fine and

Table 1
Mix proportions of mortar and concrete specimens (kg/m^3).

Specimen	Water	Type I 42.5 cement	Water to cement ratio	Fine aggregate	Coarse aggregate	
					5–10 mm	16–20 mm
Mortar	364	910	0.4	901	–	–
Concrete	222	554	0.4	541	433	649

coarse aggregates accounted for 20% and 40%, respectively. The chemical composition of the Type I 42.5 cement, the properties of the manufactured sand and crushed granite, such as the grading, silt content, apparent density, and so on, can be found in our previous paper [26]. The weight ratio of water: cement: fine aggregate in the concrete was approximate 0.4: 1: 1. The mortar with a similar weight ratio of water: cement: fine aggregate was also used as reference. Using the mix proportions shown in Table 1, the mortar and concrete were prepared and casted into the specimens with a size of $100 \times 100 \times 100$ mm^3. The specimens were demoulded after 1 day, and cured in a saturated calcium hydroxide solution at 23 °C for 28 days until testing.

2.2. 3D-DIC measurement

After curing in a saturated calcium hydroxide solution for 28 days, the mortar and concrete specimens were cut into slices with a size of $100 \times 100 \times 10$ mm^3. Then, the mortar and concrete slices were sprayed with stochastic speckle patterns, and stored under drying conditions (20 °C and 40% RH) for the 3D-DIC measurement with a displacement standard deviation of less than 0.5 μm. More details of the 3D-DIC set-up can be found in our previous study [26]. The drying-induced non-uniform deformations of the mortar and concrete slices were captured on day 1, day 3, day 7, day 14, day 28, and day 60.

2.3. Fluorescent epoxy impregnation measurement

After the 3D-DIC measurement at day 60, the concrete slice was placed in a vacuum chamber (vacuum pressure = 0.1 MPa) for 30 min to remove the air. Immediately afterwards, the concrete slice was immersed into fluorescent resin for 30 min inside a vacuum chamber to ensure that fluorescent resin was injected into the cracks of the concrete slice. Next, the concrete slice was stored under constant temperature conditions (temperature = 20 °C) until the fluorescent resin hardened. Subsequently, the concrete slice injected with fluorescent resin was polished using sandpaper with a grit size of 60, 400, and 800, respectively. Eventually, the cracking patterns of the polished concrete slice were observed using a fluorescence microscope (SteREO Discovery. V12, ZEISS, Germany).

2.4. Mechanical properties

The mechanical properties of aggregate and mortar were determined and used as inputs for the lattice fracture model. The mechanical properties of concrete were also measured. The static elastic modulus and compressive strength of the aggregates were measured using a nanoindenter (NHT3, Anton Paar, Germany). The loading and unloading were set at 3 mN/min. The maximum load was 10 mN and held for 5 s. The compressive strength and static elastic modulus of the mortar and concrete after curing for 28 days in the saturated calcium hydroxide solution were determined based on the GB T50081-2002 standard [30]. Cubic samples of $100 \times 100 \times 100$ mm^3 were used for the measurements.

3. Simulation approaches

The lattice fracture model has been extensively used for simulating the fracture process of cement-based materials [31,32]. Recently, Qian

et al. [32] developed a lattice fracture model called the generalized lattice analysis kernel (GLAK) to simulate the fracture process of cement paste. This model has been used to predict the mechanical properties of paste, mortar, and concrete [19], and the cracking of cement-based materials [16–18,33–35]. This study used the GLAK to simulate the drying-induced non-uniform deformations, stresses, and crack propagation in concrete. As shown in Fig. 1, the main inputs for the GLAK involve the lattice mesh of concrete, imposing the drying shrinkage force on the lattice mesh, and the boundary conditions. The main outputs include the bulk shrinkage of concrete, non-uniform deformations and stresses, and crack propagation in concrete. The details of the simulation process are presented below.

3.1. Digitized meso-structure of concrete

Generally, the drying-induced moisture gradient exists in concrete until the concrete is in equilibrium with the environment. Luković et al. [16] and Maruyama et al. [27] reported that the moisture gradient in concrete, which was simulated using moisture transport models, can be used to simulate and analyse the strain gradient in concrete structures. In this study, the surface deformations of the concrete slice were measured using 3D-DIC. To validate the lattice fracture model according to the 3D-DIC results, the surface layer (thickness = 0.4 mm) of the concrete slice was considered in the simulation with the lattice fracture model. It was assumed that this surface layer does not have a moisture gradient across its thickness.

To generate the lattice mesh of the concrete slice's surface layer for the lattice fracture model, the first step is to obtain the digitized meso-structure of the concrete slice's surface layer. This digitized meso-structure was obtained from the 3D-DIC photo. As shown in Fig. 2a, it was found that the coarse aggregate can be distinguished from the mortar phase in the photo of the concrete's minimum principal strain measured by 3D-DIC. By changing the colour of the aggregate to black

(RGB value: 0, 0, 0) and the colour of mortar to white (RGB value: 255, 255, 255), the digitized meso-structure of the concrete slice's surface layer could be obtained (Fig. 2b).

3.2. Lattice mesh of concrete

The digitized meso-structure of the concrete slice's surface layer was divided into 250×250 square grids with a length of $A = 0.4$ mm. As shown in the schematic representation in Fig. 3, a sub-cell with a length of $S(S = A/2)$ was assigned to the centre of each square. Subsequently, a node was randomly generated in each sub-cell. Depending on the main phase in the square grids, each node was designated either as an aggregate node or mortar node. Then, the beams for the lattice fracture model were generated by connecting the nodes using the Delaunay triangulation algorithm.

According to the type of connected nodes, the beams can be categorized into three types: the beam that connects two mortar nodes is defined as mortar beam, the beam that connects two coarse aggregate nodes is defined as coarse aggregate beam, and the beam that connects one mortar node and one coarse aggregate node is defined as interface beam. Fig. 4 shows the established lattice mesh.

According to the experiments in Section 2.4, the compressive strength of mortar and concrete after curing for 28 days in the saturated calcium hydroxide solution were 42.0 ± 0.7 MPa and 51.5 ± 4.8 MPa, respectively. Table 2 lists the mechanical properties of different beam types, which were used as inputs for the lattice fracture model. The elastic modulus of the aggregate and mortar beams were obtained through experiments. In the simulations of Luković et al. [16] and Zhang et al. [35], it was assumed that the tensile strength of cement-based materials were 1/10 times the compressive strength of cement-based materials. In current study, the method of Luković et al. [16] and Zhang et al. [35] was also used to calculate the tensile strength of coarse aggregate and mortar. The mechanical property values of the interface
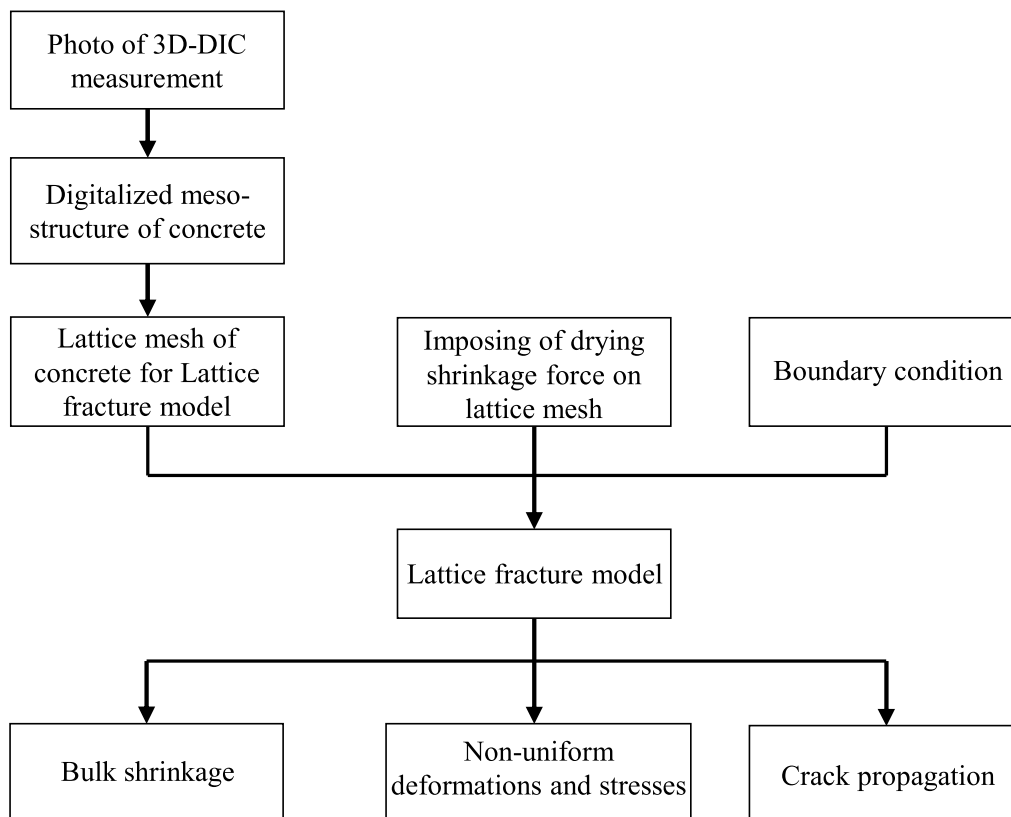

Fig. 1. Outline of simulation of drying-induced non-uniform deformations, stresses, and crack propagation in concrete using GLAK.
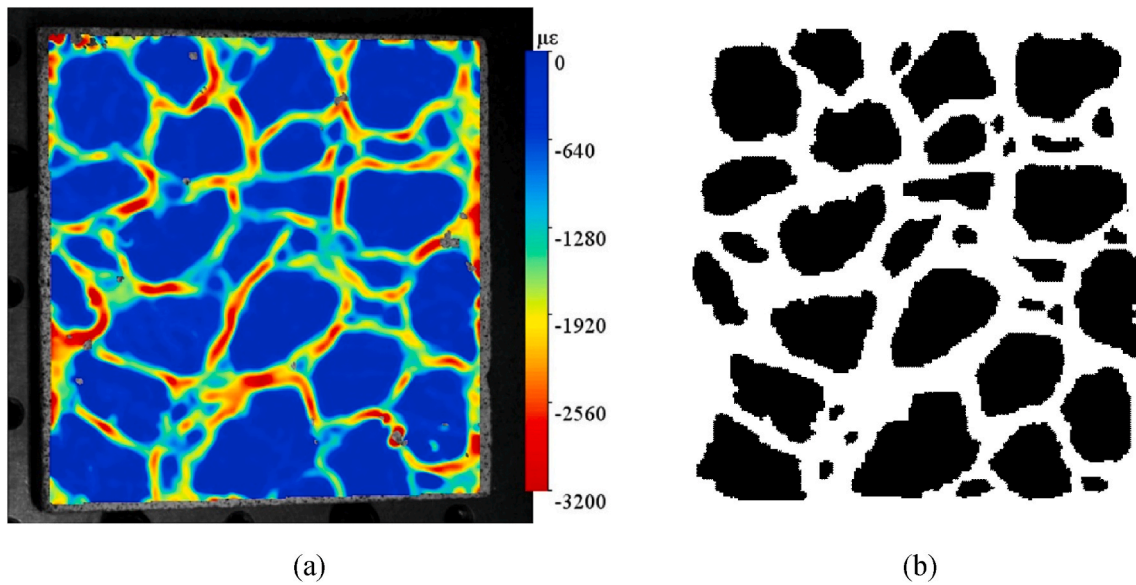
Fig. 2. Digitized meso-structure of concrete slice's surface layer from 3D-DIC measurement: (a) photo of minimum principal strain of concrete slice obtained by 3D-DIC measurement; (b) digitized meso-structure of concrete slice's surface layer. Note: the size is 100×100 mm^2.
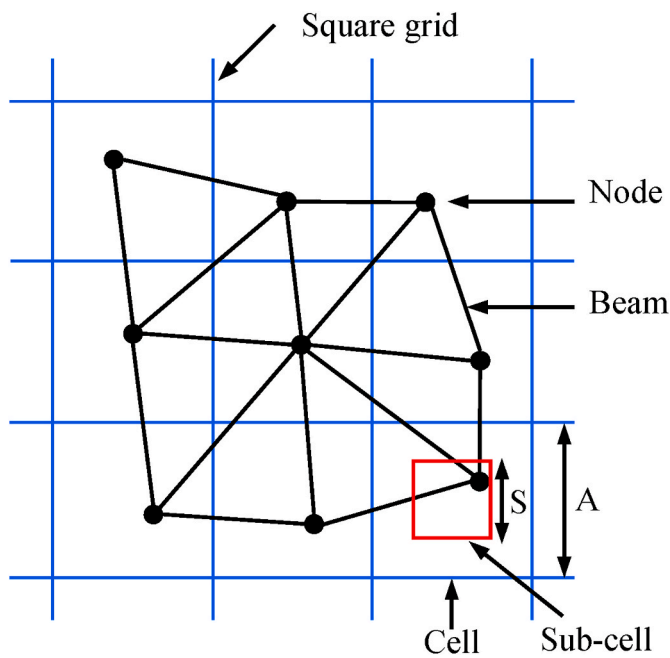

Fig. 3. Schematic representation of establishing lattice mesh for lattice fracture model.

beams were obtained from Luković et al. [16]. Notably, the interface beams did not represent the interfacial transition zone (ITZ) in concrete, because the thickness of ITZ is normally less than 50 μm, while the length of interface beams was around 0.4 mm. To some extent, however, the influence of ITZ on the drying-induced deformations of concrete was considered in current simulation, because the mechanical properties of interface beams were much smaller than that of coarse aggregate and mortar beams.

3.3. Imposing drying shrinkage force on lattice mesh

Under drying conditions, the moisture in the mortar phase of the concrete is transported to the environment until the mortar phase and the environment are in equilibrium. The change of moisture in the mortar phase leads to the drying shrinkage of the mortar phase, which exerts a drying shrinkage force to the concrete. According to the abovementioned mechanism, this study proposed an iteration algorithm to impose the drying shrinkage force (N_{sh}) onto the lattice mesh of concrete as follows. At step i, a shrinkage force (N_i) is imposed on all mortar beams. Consequently, the mortar beams shrink and the shrinkage is restrained by the other beams, which causes the formation of tensile force in some beams in the system. Then, the lattice fracture model searches for the beam with the highest ratio of tensile force to tensile strength. The shrinkage force N_i increases until the beam with the highest ratio of tensile force to tensile strength is broken. This iteration algorithm continues until the shrinkage force N_i increases to the shrinkage force N_{sh}.

According to Luković et al. [16], the drying shrinkage force N_{sh} can be calculated as follows:

$$N_{sh} = \varepsilon_{sh} E_m A \tag{1}$$

where ε_{sh} is the drying shrinkage of the mortar phase in the surface layer of the concrete slice, E_m is the elastic modulus of the mortar phase, and A is the area of the beams' cross-section.

To calculate the ε_{sh} of mortar phase, it was assumed that, for the mortar phase in the concrete slice, the rate of moisture transport to the environment was close to that for the mortar slice under the same drying conditions. Hence, the mortar phase in the surface layer of the concrete slice was assumed to have the same moisture as the surface layer of the mortar slice with the same drying time. Thus, the ε_{sh} of mortar phase was assumed as equal to the drying shrinkage of the mortar slice's surface layer, which can be experimentally measured using 3D-DIC.

Table 3 lists the ε_{sh} values of the mortar slice's surface layer obtained using the 3D-DIC method. It was found that ε_{sh} increased from 561 μm/m on day 1–1643 μm/m on day 60. Moreover, N_{sh} increased from 1.52×10^{-3} kN on day 1–4.44×10^{-3} on day 60, and the calculated drying shrinkage stress increased from 11.5 MPa on day 1–33.7 MPa on day 60. According to these results, the moisture in the mortar and concrete specimens were not in equilibrium with the environment (20 °C and 40% RH) at 60 days since drying. Wu et al. [36] reported that the moisture equilibrium between the concrete and the environment of 21 °C and 55 %RH would take 10 months. In current study, a drying time longer than 60 days was not used, because the focus of this study was not on the transport of moisture from concrete to environment. According to
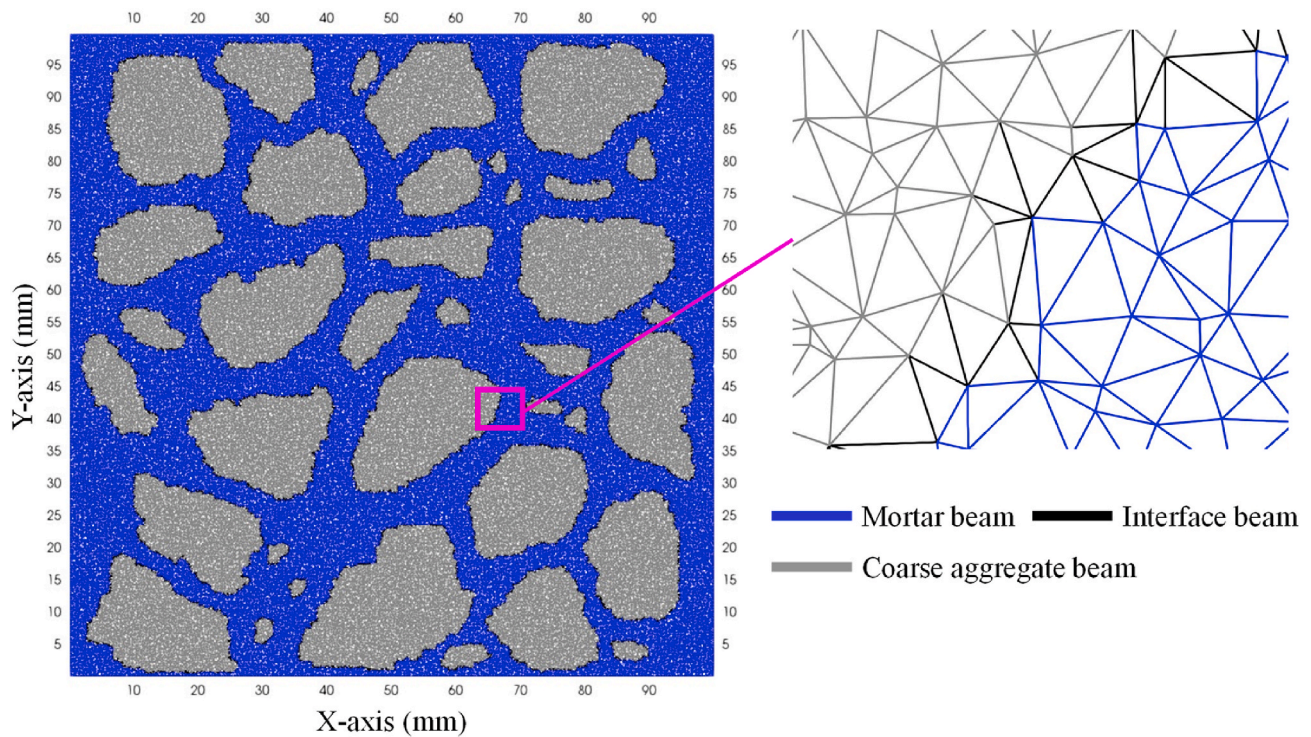
Fig. 4. Established lattice mesh of concrete slice's surface layer for lattice fracture model.

Table 2
Mechanical properties of different beam types.

	Elastic modulus (GPa)	Compressive strength (MPa)	Calculated tensile strength (MPa)
Coarse aggregate beam	80.0	90.0	9.0
Mortar beam	20.5	42.0	4.2
Interface beam	15.0	25.0	2.5

Table 3
Drying shrinkage force (N_{sh}) imposed on the mortar beams.

Time since drying (days)	ε_{sh} of mortar (μm/m)	E_m (GPa)	A (mm²)	N_{sh} (kN)	Stress (MPa)
1	561	20.5	0.205	1.52×10^{-3}	11.5
3	926	20.5	0.205	2.50×10^{-3}	18.9
7	1129	20.5	0.205	3.05×10^{-3}	23.1
14	1277	20.5	0.205	3.45×10^{-3}	26.2
28	1470	20.5	0.205	3.97×10^{-3}	30.1
60	1643	20.5	0.205	4.44×10^{-3}	33.7

Note: stress $= \varepsilon_{sh} \times E_m$

our preliminary experiments, significant micro-cracks can be observed on the surface of concrete specimens under drying at 20 °C and 40% RH for 60 days, which are adequate for analysing the influence of non-uniform deformation and stress on the drying-induced micro-cracks in concrete.

3.4. Boundary conditions

To compare the experimental and simulation results, fours nodes were fixed at the centre of the lattice mesh. Thus, the other nodes moved toward the centre when the drying shrinkage force was applied in the lattice fracture model simulation.

4. Results and discussion

4.1. Non-uniform deformation

In the 3D-DIC measurement, by comparing the images captured before and after the deformations, the deformation fields in the X-, Y- and Z-axis can be obtained and used to calculate the normal, shear, and principal strains [21]. This study focused on the deformation fields in the directions of the X- and Y-axis. The left side of Fig. 5 shows the measured deformation fields in the direction of the X-axis from day 1 to day 60. As can be seen, the deformation fields are non-uniform, owing to the restriction of aggregates. In some areas, such as the area marked with an arrow in the 60-day image (bottom left in Fig. 5), the deformations did not exhibit significant differences because aggregates were located in these areas. As the coordinates along the X-axis increased, the deformations changed from positive to negative, which demonstrates that the drying-induced deformations moved toward the centre of the concrete slice. The simulated deformation fields in the direction of the X-axis from day 1 to day 60, which are shown on the right side of Fig. 5, were smoother compared with those measured using 3D-DIC. Particularly, the aggregate areas, such as the area marked with an arrow in the 60-day image shown at the bottom right of Fig. 5, had the same deformation, which is consistent with the results obtained by the 3D-DIC measurement.

Fig. 6 shows the comparison between the measured (left side) and simulated (right side) displacement fields in the direction of the Y-axis. Similar to the displacement fields in the direction of the X-axis, both the measured and simulated displacement fields in the direction of Y-axis indicate that the drying-induced.
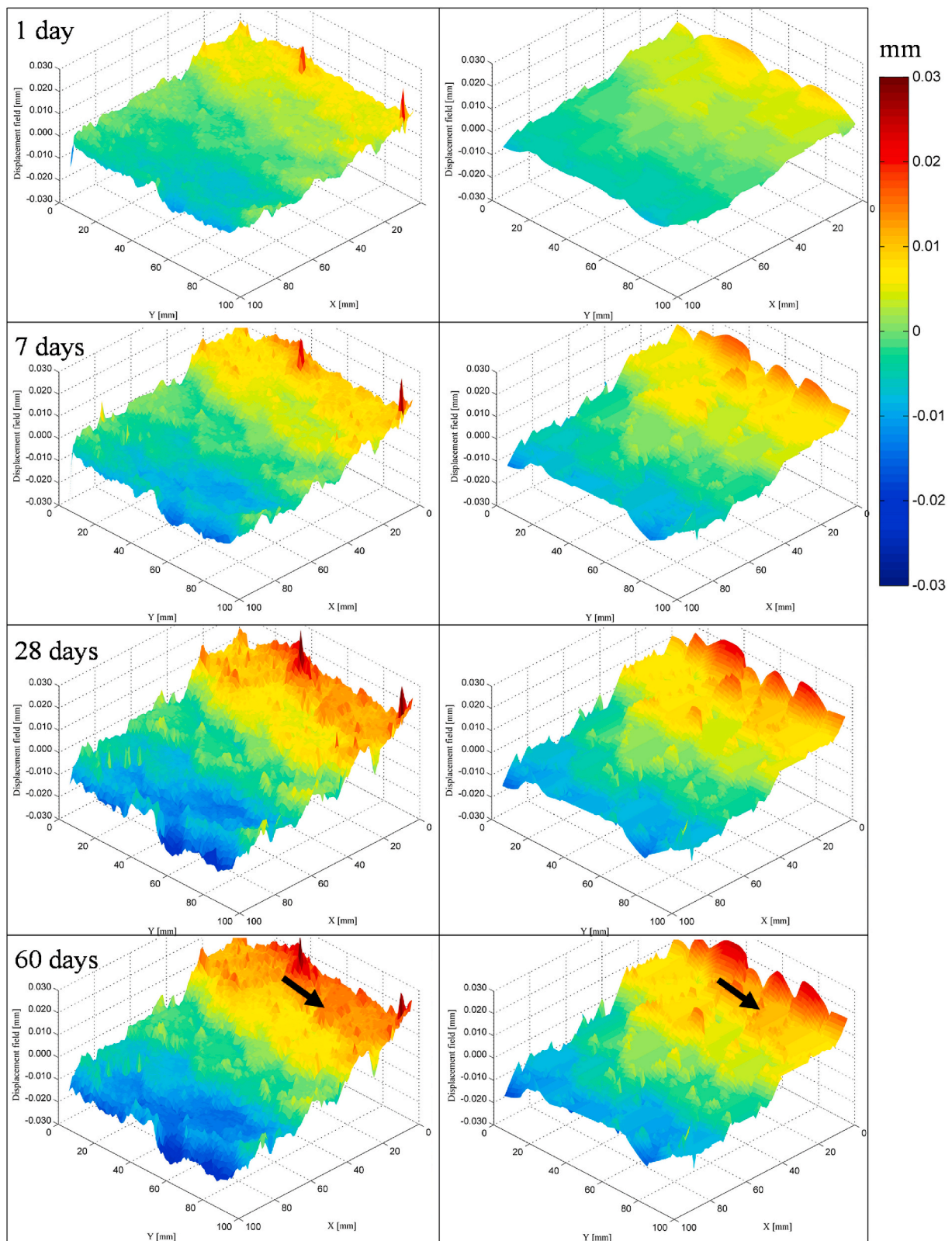
Fig. 5. Displacement fields in direction of X-axis: 3D-DIC measurement (left) versus lattice fracture simulation (right).

deformations moved toward the centre of the concrete slice. Additionally, the displacement fields in the Y direction were non-uniform. Some areas, such as the area marked with an arrow in the 60-day image, had similar deformations because the phases in these areas were aggregates.

For a more direct comparison of the non-uniform deformations obtained using the 3D-DIC measurement and lattice fracture model, two perpendicular lines, namely, X50 (the equation is y = 50 mm and x ranges from 0 to 100 mm) and Y50 (the equation is x = 50 mm and y ranges from 0 to 100 mm) were considered. As shown in Fig. 7a and b,
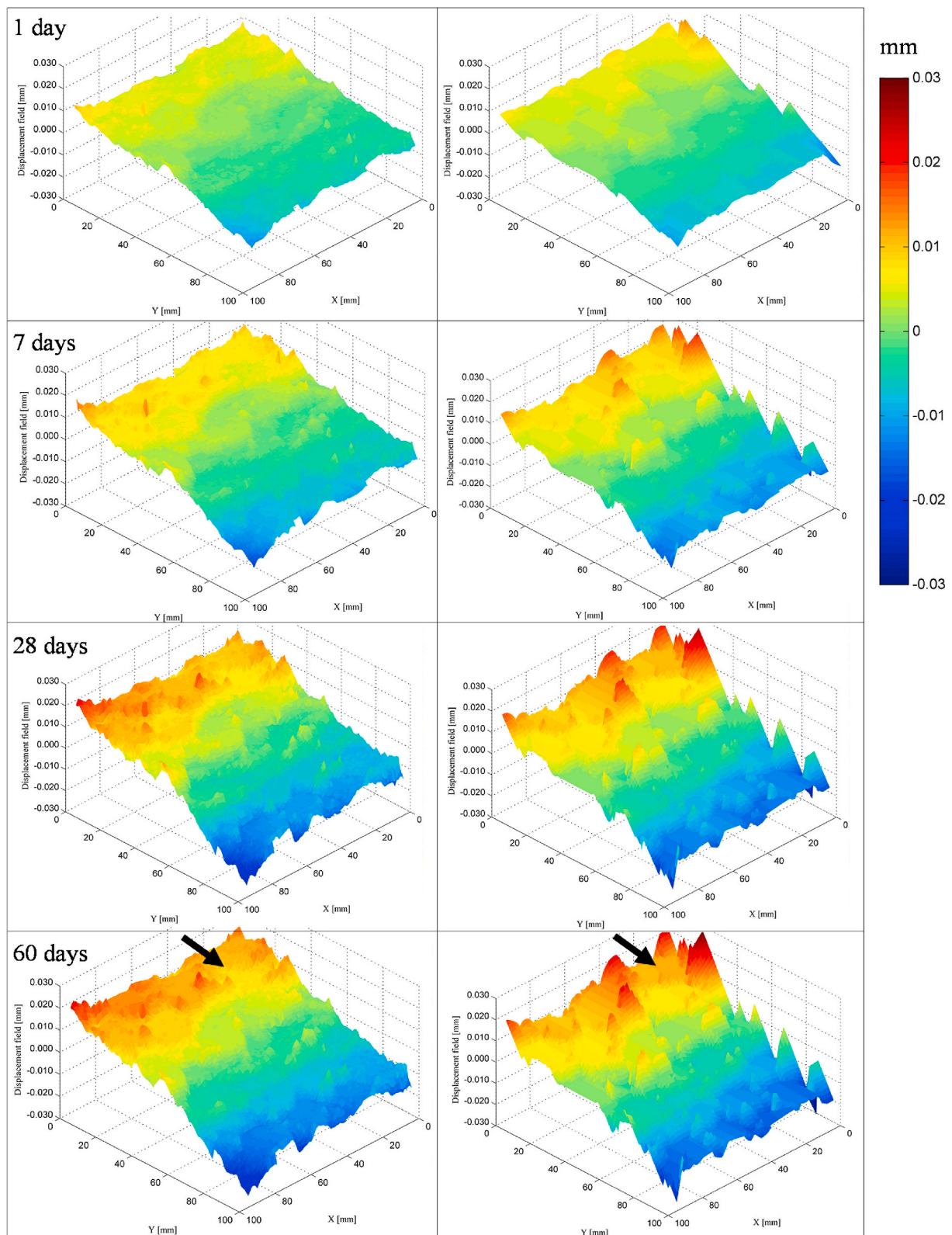
Fig. 6. Displacement fields in direction of Y-axis: 3D-DIC measurement (left) versus lattice fracture simulation (right).

X50 and Y50 were divided into 11 segments (x1 to x11 and y1 to y11) according to the phases in the lines, respectively. As shown in Fig. 7a, the simulation results of the lattice fracture model revealed that the displacements slightly changed in the aggregate segments (x2, x4, x6, x8, and x10). In most mortar segments (x1, x5, x9, and x11), the displacements seem to have linearly decreased with the increase of the

coordinate. At the boundaries between the mortar and aggregate phases, the displacements did not significantly fluctuate because the deformations of the mortar and aggregate phases were also distinct, which may result in micro-cracks at the interface. Moreover, displacement fluctuations were also observed in mortar segments with a large length (x3 and x7). This is attributed to the formation of micro-cracks in the
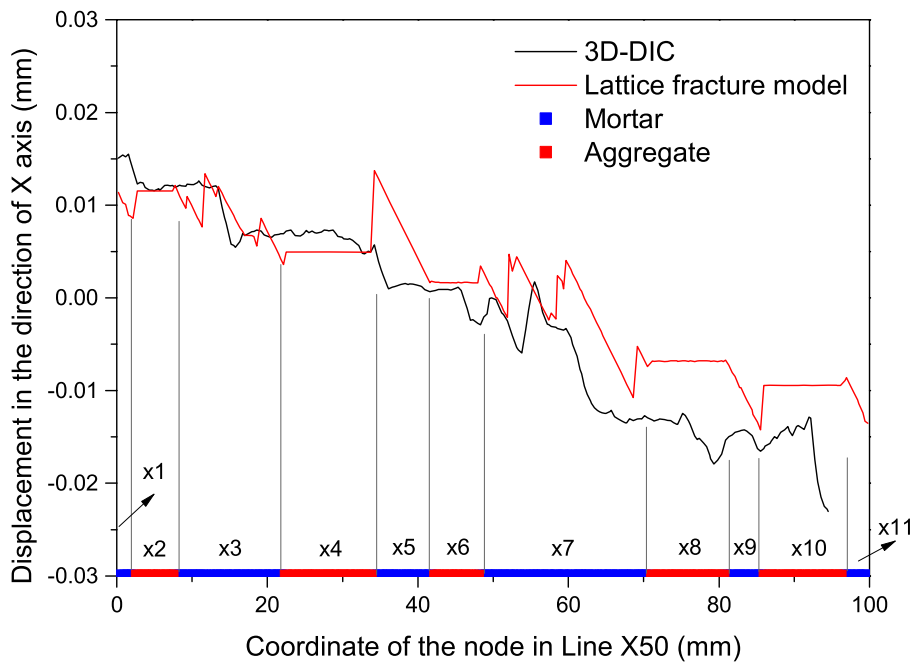
(a) Displacement field in line X50.
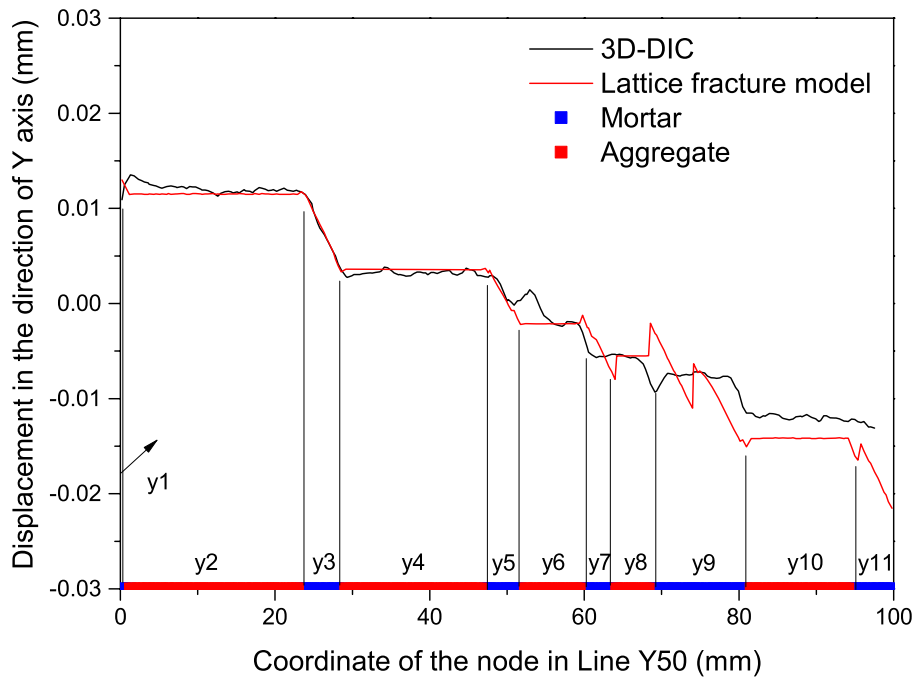
(b) Displacement field in line Y50.

Fig. 7. Displacement fields along X50 and Y50 (the nodes in the lines represent the mortar and aggregate).

mortar phase. The abovementioned trends in the simulation results are consistent with the 3D-DIC measurement. According to the simulated displacement fields along the Y50 line shown in Fig. 7b, it is more obvious that the displacements levelled off in the aggregate segments, and decreased in the mortar segments. From the abovementioned results and analysis, it was concluded that the simulated drying-induced non-uniform deformations in the concrete slice are in good agreement with those measured using 3D-DIC.

As shown in Fig. 8, the measured bulk drying shrinkage of the

concrete slice's surface layer increased from approximately 150 μm/m on day 1 to approximately 350 μm/m on day 60. The simulated bulk drying shrinkage of the concrete slice's surface layer was close to the 3D-DIC measurement at an early age, but was slightly smaller than that obtained using 3D-DIC at a later age. As will be discussed in Section 4.3, this difference may have been caused by creep.
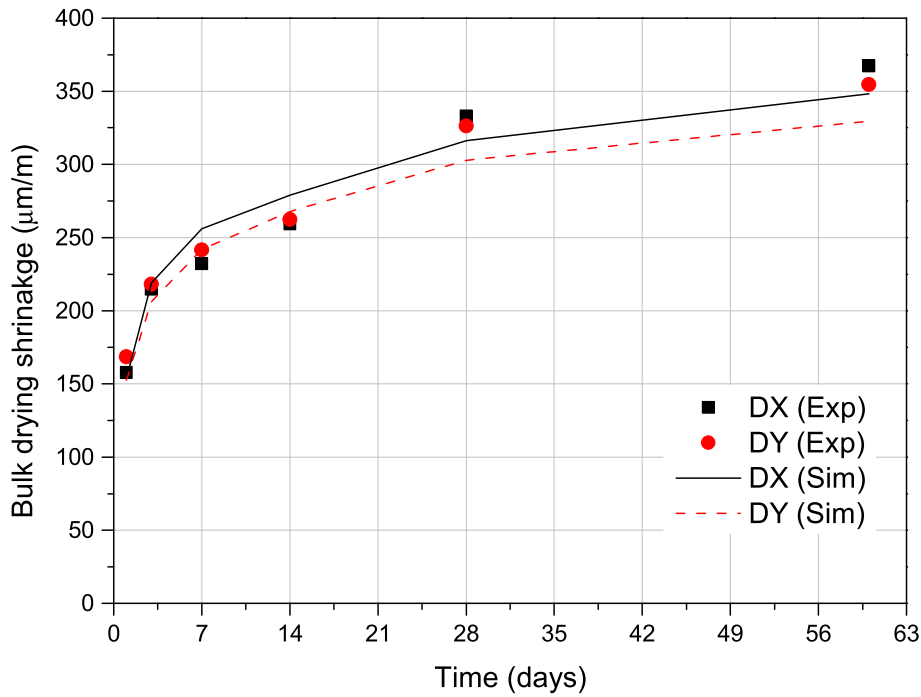
Fig. 8. Bulk drying shrinkage of concrete slice's surface layer in X and Y directions obtained by 3D-DIC and lattice fracture model. DX = Direction of X-axis, DY = Direction of Y-axis, Exp = Experiment, Sim = Simulation.

4.2. Micro-crack propagation

Fig. 9 shows the development of the dying-induced micro-cracks in the concrete slice dried at day 1 and day 60, as simulated using the lattice fracture model. Fig. 10 shows the simulated and measured cracking patterns of the concrete slice after drying for 60 days. As shown in Figs. 9 and 10, the simulated micro-cracks can be categorized in two types: micro-cracks in the mortar phase and micro-cracks at the interface. It appears that the micro-cracks in the mortar phase propagated perpendicularly to the aggregates, while the micro-cracks at the interface developed parallel to the aggregates. This is in good agreement with the results of the fluorescent epoxy impregnation measurement (Fig. 10). Moreover, the micro-crack patterns are consistent with the

abovementioned non-uniform deformation trends (Fig. 7), and the fluctuations in the deformation fields of the concrete slice can be categorized into two types: fluctuations around the interface between the mortar and the aggregate phases, and fluctuations in the mortar phase, for which the adjacent aggregates have a long distance. These two types of micro-cracks have been previously reported by Slate and Olsefski [37], Goltermann [28], and Maruyama and Sasano [6], for example. By using classical elasticity theories, Goltermann [28] calculated the stresses of the cement paste embedded with a spherical aggregate. It was found that the restraint of aggregate on the shrinkage of cement paste resulted in the tangential tensile stresses in the cement paste, which caused the radial micro-cracks. Shear stresses were also found along the interface and could lead to the micro-cracks parallel to the surface of
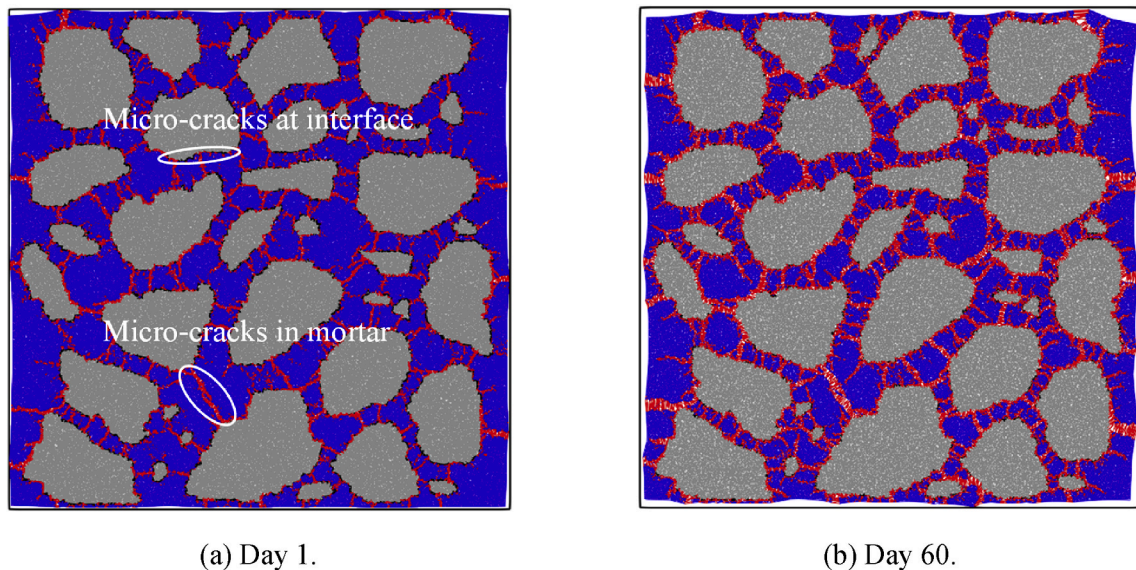

(a) Day 1.

(b) Day 60.

Fig. 9. Simulated drying-induced micro-crack propagation in surface layer of concrete slice that dried at day 1 and day 60. Note: the deformations are magnified 80 times for visualization purposes.
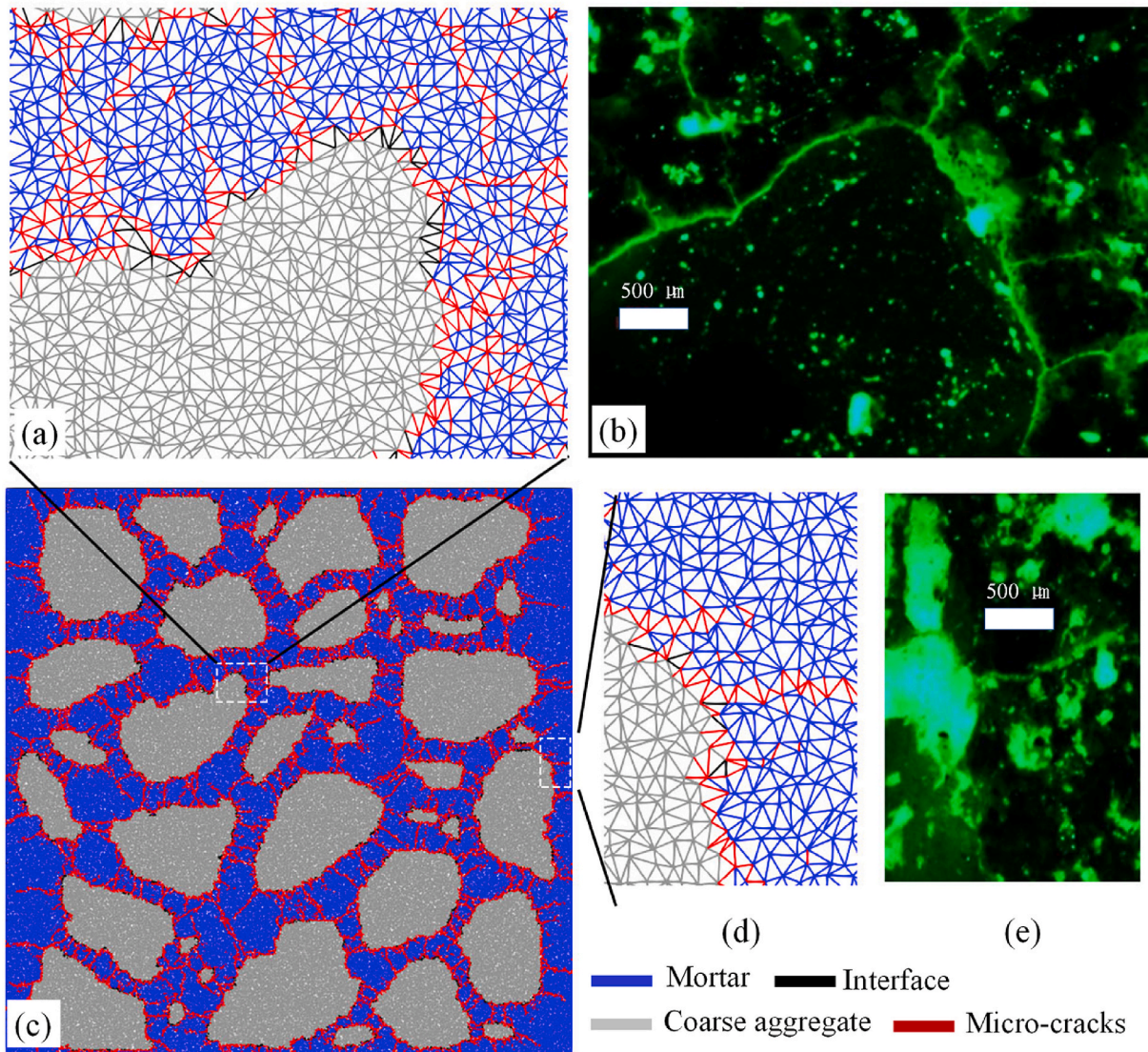
Fig. 10. Micro-crack patterns obtained by lattice fracture simulation and fluorescent resin measurement for concrete that dried for 60 days: (a), (c) and (d) are patterns obtained by the lattice fracture model; (b) and (e) are the patterns obtained by the fluorescent resin measurement. Note: the deformation is not magnified.
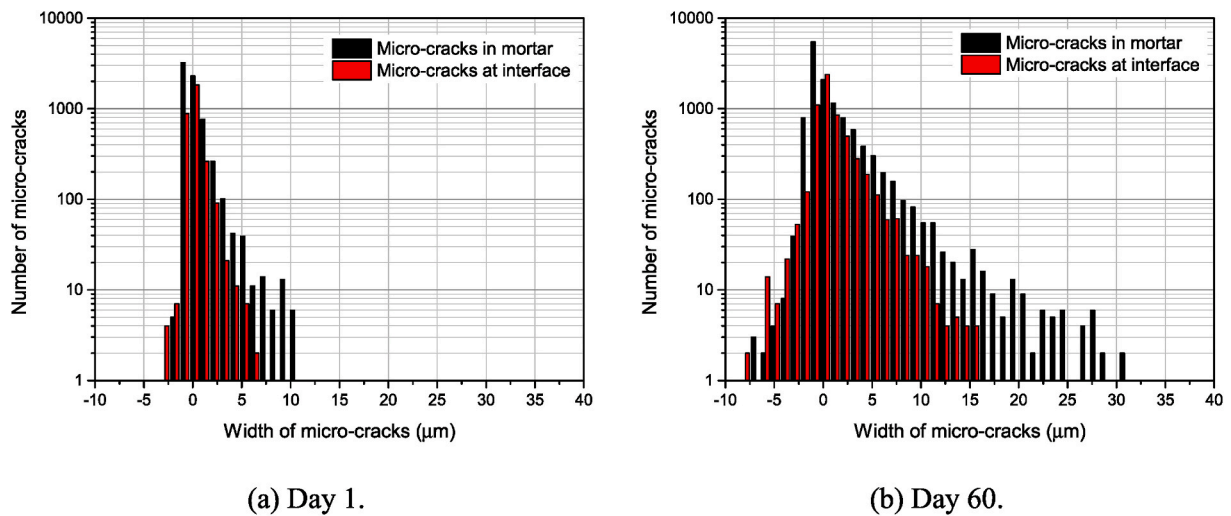

Fig. 11. Simulated width distribution of two micro-crack types at day 1 and day 60. Note: the width of the micro-cracks is calculated as the distance between the two nodes in a cracked beam.

aggregate. Further, Maruyama and Sasano [6] indicated that the mortar surrounded by several aggregates with small distance could shrink toward the centre of the mortar, which might cause the formation of micro-cracks along the interface.

According to Fig. 9b, the micro-cracks in the mortar phase appear to be wider than those at the interface. To analyse this difference, the width distribution of these two micro-crack types was plotted as shown in Fig. 11. As can be seen, the maximum width of the mortar micro-cracks is larger than that of the interface micro-cracks. From day 1 to day 60, the maximum width of the mortar micro-cracks increased from 15.5 μm to 34.9 μm, while that of the interface micro-cracks increased from 6.3 μm to 15.5 μm. Moreover, the number of mortar micro-cracks was approximately twice that of the interface micro-cracks for each age. Fig. 12a shows the number of micro-cracks in the mortar and interface beams for the different drying shrinkage stresses imposed onto the mortar. Obviously, the number of micro-cracks in the mortar beams had a higher increase rate as the imposed drying shrinkage stress increased. As shown in Fig. 12b, both of the maximum micro-crack widths in the mortar and at the interface are proportional to the drying shrinkage stress N_{sh} imposed on the mortar beams. Additionally, the maximum micro-crack width in the mortar had a higher rate of increase. The abovementioned results indicate that the drying-induced micro-cracking in the mortar phase is more alarming compared with the micro-cracking at the interface. Based on the calculation of classical elasticity theories, Goltermann [28] also found that the drying-induced micro-cracks along the interface were very thin.

4.3. Non-uniform stress

The driving force of drying shrinkage in concrete changes with ongoing drying, which affects the non-uniform stresses in concrete. In addition, the non-uniform stresses might be redistributed due to the formation of micro-cracks. This could affect the formation of new micro-cracks in further drying process. In the studies like Goltermann [28], the non-uniform stresses at the initial stage of drying were calculated and used to analyse the formation of micro-cracks. However, the interaction between non-uniform stresses and micro-cracks was not clarified because the evolution of non-uniform stresses was not captured. In current study, the non-uniform stresses in concrete were captured using the lattice fracture model. Since the lattice fracture model was validated by the comparison of non-uniform deformations and micro-cracks between experiments and simulation, the non-uniform stresses captured using the lattice fracture model were relatively reliable. In this section, the interaction between non-uniform stresses and micro-cracks is discussed and analysed as follows.
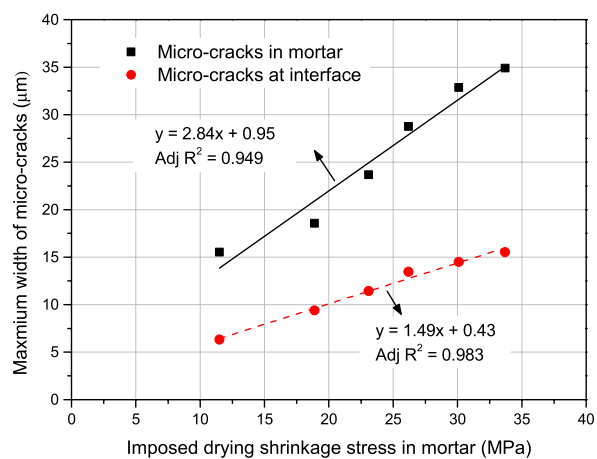
Fig. 13 shows the stress fields in the mortar phase of the concrete slice under drying at very early age (the imposed drying shrinkage pressure was 1.81 MPa and only 100 beams broke), 1 day and 60 days. As shown in Fig. 13a and d, radial compressive stresses and tangential tensile stresses were formed in the mortar that covered coarse aggregate. These compressive stresses were mainly caused by the restraint of coarse aggregate on the shrinkage of mortar phase, and consistent with the calculation by Goltermann [28]. The tangential tensile stresses could lead to the formation of micro-cracks in the mortar phase, e.g. in area I and II. As drying continues and the formation of micro-cracks, both the compressive and tensile stresses in the mortar phase changed. The compressive stresses concentrated around the micro-cracks, while the tensile stresses concentrated in the area surrounded by the micro-cracks. For example, as shown in Fig. 13e, area III located between area I and II. Due to the formation of micro-cracks in area I and II, the continuity of the mortar that covered coarse aggregate was broken at day 1. Consequently, the restraint of coarse aggregate on the shrinkage of mortar phase was reduced around the micro-cracks. However, the restraint of coarse aggregate on the shrinkage of mortar phase remained in the area without micro-cracks. Hence, area III showed high tensile stresses. Consequently, new micro-cracks were formed in area III with further drying to day 60 (see Fig. 13f). Also, it can be imagined that area IV in Fig. 13f could appear microcracking as drying continues.

Fig. 14 presented the stress fields in the coarse aggregate of the concrete slice. As shown in Fig. 14a, the coarse aggregate was mainly in hydrostatic compression at very early age. This was due to the reaction force of the restraint of coarse aggregate on the shrinkage of mortar phase, and was also consistent with the calculation by Goltermann [28]. Very small part of the coarse aggregate was in tension (Fig. 14d). This was probably caused by the shrinkage of the mortar that surround by coarse aggregates [6]. As aforementioned, the formation of micro-cracks could reduce the restraint of coarse aggregate on the shrinkage of mortar phase. Thus, the reaction force of the restraint of coarse aggregate on the shrinkage of mortar phase could be reduced around the micro-cracks. Hence, as can be seen from Fig. 14b and c, the compressive stresses in the coarse aggregate were released particularly around the area where the microcracking occurred (e.g. area V). Notably, the distribution of tensile stresses was influenced by the formation of micro-cracks. As can be seen from area V in Fig. 14e and f, tensile stresses were formed in the coarse aggregate due to the shrinkage of mortar phase around the micro-cracks. Since the cement-based materials normally show much smaller tensile strength than compressive strength, these tensile stresses seem to increase the cracking risk of coarse aggregate. This mechanism
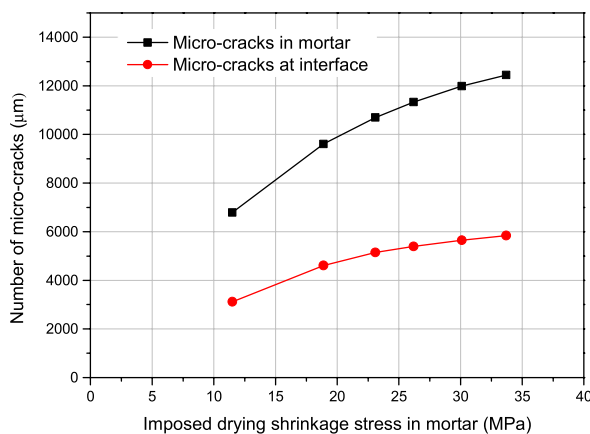
(a) Number of micro-cracks.

(b) Maximum width of micro-cracks.

Fig. 12. Number and maximum width of micro-cracks in mortar and interface beams versus imposed drying shrinkage stresses in the mortar phase.
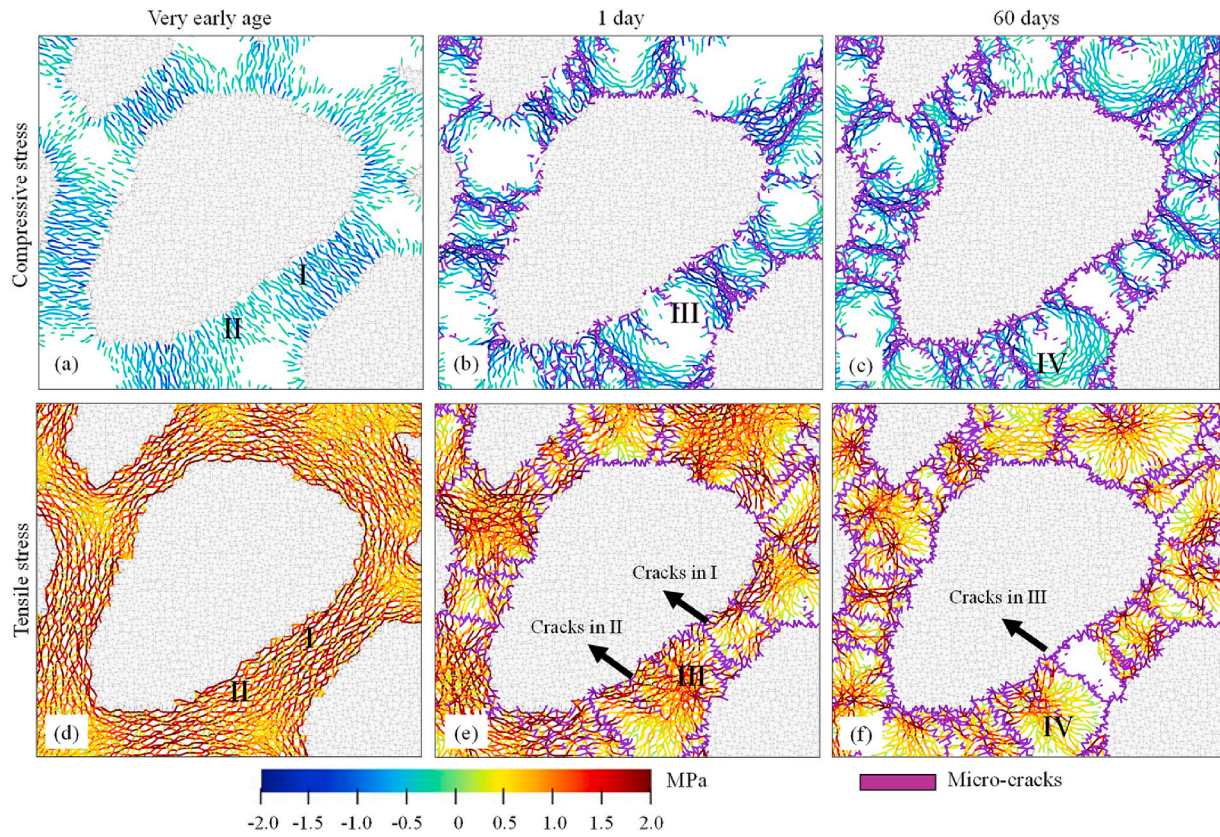
Fig. 13. Stress fields in the mortar phase of the concrete slice: (a) and (d) are for the drying at very early age (the imposed drying shrinkage pressure was 1.81 MPa and only 100 beams broke); (b) and (e) are for the drying at 1 day; (c) and (f) are for the drying at 60 days.

Fig. 14. Stress fields in the coarse aggregate of the concrete slice: (a) and (d) are for the drying at very early age (the imposed drying shrinkage pressure was 1.81 MPa and only 100 beams broke); (b) and (e) are for the drying at 1 day; (c) and (f) are for the drying at 60 days.
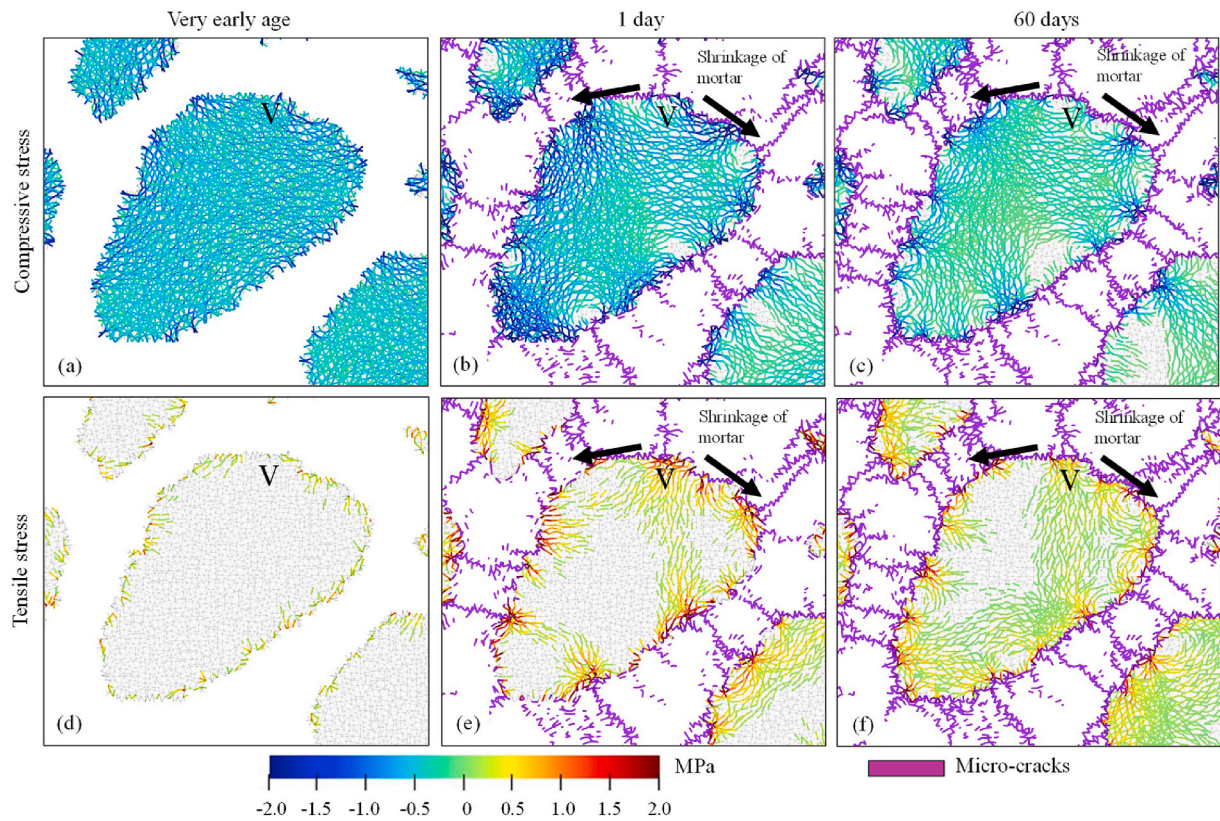
could be used to illustrate the propagation of drying-induced micro-cracks across aggregates observed in the studies like Wu et al. [36].

Based on the above analysis, the formation of micro-cracks reduces the restraint of coarse aggregate on the shrinkage of mortar phase. Consequently, the tensile stresses in the mortar phase tend to concentrate in the centre of the area that is surrounded by micro-cracks, which lead to the formation of new micro-cracks as drying continues. Also owing to the formation of micro-cracks, tensile stresses rise in coarse aggregate and could cause high cracking risk. This study clarified the interaction mechanism between drying-induced micro-cracks and non-uniform stresses in concrete, which is promising for evaluating the effect of aggregate properties on the drying-induced micro-cracks in concrete, since the non-uniform stresses in concrete are correlated with the volume, size, shape and so on of aggregates. In addition, the application of DIC in capturing drying-induced non-uniform deformations in concrete is also attractive for the validation of other structure models.

Notably, the drying creep must be considered to predict the drying-induced shrinkage in cement-based materials, because these materials exhibit the viscoelastic effect [38,39]. As summarized by Bažant and Jirásek [39], the occurrence of drying creep has two causes: the increase of the rate of bond fractures in the C–S–H gel at the nanoscale, owing to the effect of local stress increase caused by the drying process, and the drying-induced micro-cracks, which are considered as drying creep for convenience. This study quantified the contribution of the drying-induced micro-cracks to the drying creep, because the propagation of micro-cracks was involved in the lattice fracture model to simulate the non-uniform deformation of concrete (Figs. 9 and 10). Additionally, the contribution of the C–S–H gel's deformation to creep was partially considered. The drying shrinkage of mortar measured using the 3D-DIC method, which were used as the inputs for calculating the drying shrinkage force imposed onto the lattice mesh, includes the drying creep caused by the deformation of the C–S–H gel. However, the drying creep behaviour of the mortar phase in the concrete slice was different to that of the mortar slice, because the stress field in the mortar phase of the concrete slice was significantly influenced by the aggregate restraints (see Fig. 13a and d). Moreover, the drying shrinkage force in the mortar phase changed until the mortar phase and the environment were in equilibrium, and micro-cracks were generated owing to the stress fields formed in the concrete (see Fig. 13e and f). Thus, the stress fields in the concrete components changed dynamically as the drying process advanced. Further work should focus on quantifying the effect of non-uniform stresses on the drying-creep.

5. Conclusions

From the validation results for the lattice fracture model, and the analysis of the correlation between the drying induced stresses and micro-crack propagation in the concrete, the following conclusions can be drawn:

(1) The drying-induced non-uniform deformations, stresses, and micro-cracks in concrete were simulated using the lattice fracture model, wherein the drying shrinkage force was imposed on the mortar phase with an iteration algorithm. The non-uniform deformations from the simulation were in good agreement with that captured using the 3D-DIC. Also, the simulated propagation of micro-cracks was consistent with the observation of fluorescent epoxy impregnation method. Based on the above two aspects, the lattice fracture model was validated for simulating the drying-induced non-uniform behaviours in concrete, illustrating that the non-uniform stresses obtained using the lattice fracture model was relatively reliable. The DIC technique is also attractive for the validation of other structure-based models.

(2) The interaction between the drying-induced non-uniform stresses and micro-cracks in concrete was analysed. It was found that the micro-cracks broke the continuity of the mortar phase that

covered coarse aggregate, which reduced the restraint of coarse aggregate on the shrinkage of mortar phase. Tensile stresses remained high in the centre of the mortar surrounded by micro-cracks, leading to the formation of new micro-cracks with ongoing drying. In the coarse aggregate, where was close to the radial micro-cracks formed in the mortar phase, high tensile stresses were caused by the shrinkage of the mortar that covered coarse aggregate. These high tensile stresses could cause micro-cracking across coarse aggregate.

Declaration of competing interest

The authors declare that they have no known competing financial interests or personal relationships that could have appeared to influence the work reported in this paper.

Acknowledgements

References

[1] W. Hansen, Constitutive Model for predicting ultimate drying shrinkage of concrete, J. Am. Ceram. Soc. 70 (1987) 329–332.

[2] B. Bissonnette, P. Pierre, M. Pigeon, Influence of key parameters on drying shrinkage of cementitious materials, Cement Concr. Res. 29 (1999) 1655–1662.

[3] O. Coussy, The equivalent pore pressure and the swelling and shrinkage of cement-based materials, Mater. Struct. 37 (2003) 15–20.

[4] C.M. Neubauer, H.M. Jennings, The use of digital images to determine deformation throughout a microstructure Part I Deformation mapping technique, J. Mater. Sci. 35 (2000) 5741–5749.

[5] J. Bisschop, J.G.M. van Mier, Effect of aggregates on drying shrinkage microcracking in cement-based composites, Mater. Struct. 35 (2002) 453–461.

[6] I. Maruyama, H. Sasano, Strain and crack distribution in concrete during drying, Mater. Struct. 47 (2014) 517–532.

[7] J.E. Bolander, S. Berton, Simulation of shrinkage induced cracking in cement composite overlays, Cement Concr. Compos. 26 (2004) 861–871.

[8] V. Slowik, T. Hübner, M. Schmidt, B. Villmann, Simulation of capillary shrinkage cracking in cement-like materials, Cement Concr. Compos. 31 (2009) 461–469.

[9] P. Grassl, H.S. Wong, N.R. Buenfeld, Influence of aggregate size and volume fraction on shrinkage induced micro-cracking of concrete and mortar, Cement Concr. Res. 40 (2010) 85–93.

[10] A.E. Idiart, C.M. López, I. Carol, Modeling of drying shrinkage of concrete specimens at the meso-level, Mater. Struct. 44 (2011) 415–435.

[11] A. Idiart, J. Bisschop, A. Caballero, P. Lura, A numerical and experimental study of aggregate-induced shrinkage cracking in cementitious composites, Cement Concr. Res. 42 (2012) 272–281.

[12] P. Havlásek, M. Jirásek, Multiscale modeling of drying shrinkage and creep of concrete, Cement Concr. Res. 85 (2016) 55–74.

[13] H. Samouh, E. Rozière, A. Loukili, The differential drying shrinkage effect on the concrete surface damage: experimental and numerical study, Cement Concr. Res. 102 (2017) 212–224.

[14] E. Schlangen, G. Leegwater, E.A. B Koenders, Modelling of autogenous shrinkage of concrete based on paste measurements, in: J. Marchand, B. Bissonnette, R. Gagne, M. Jolin, F. Paradis (Eds.), 2nd International Symposium on Advances in Concrete through Science and Engineering. Quebec City, Canada, RILEM Publications SARL, 2006.

[15] E. Schlangen, E.A.B. Koenders, K. van Breugel, Influence of internal dilation on the fracture behaviour of multi-phase materials, Eng. Fract. Mech. 74 (2007) 18–33.

[16] M. Luković, B. Šavija, E. Schlangen, G. Ye, K. Van Breugel, A 3D lattice modelling study of drying shrinkage damage in concrete repair systems, Materials 9 (2016) 575.

[17] L. Liu, X. Wang, H. Chen, C. Wan, Microstructure-based modelling of drying shrinkage and microcracking of cement paste at high relative humidity, Construct. Build. Mater. 126 (2016) 410–425.

[18] L. Liu, X. Wang, H. Chen, C. Wan, M. Zhang, Numerical modeling of drying shrinkage deformation of cement-based composites by coupling multiscale structure model with 3D lattice analyses, Comput. Struct. 178 (2017) 88–104.

[19] Z. Qian, Multiscale Modelling of Fracture Processes in Cementitious Materials, Dissertation, Delft University of Technology, Delft, The Netherlands, 2012.

[20] Z. Qian, E.J. Garboczi, G. Ye, E. Schlangen, Anm: a geometrical model for the composite structure of mortar and concrete using real-shape particles, Mater. Struct. 49 (2016) 149–158.

[21] E.D. Dzaye, E. Tsangouri, K. Spiessens, G. De Schutter, D.G. Aggelis, Digital image correlation (DIC) on fresh cement mortar to quantify settlement and shrinkage, Arch. Civ. Mech. Eng. 19 (2019) 205–214.

[22] P. Zhao, A.M. Zsaki, M.R. Nokken, Digital image correlation to evaluate plastic shrinkage cracking in cement-based materials, Construct. Build. Mater. 182 (2016) 108–117.

[23] Y. Zhao, L. Wang, Z. Lei, X. Han, Y. Xing, Experimental study on dynamic mechanical properties of the basalt fiber reinforced concrete after the freeze-thaw based on the digital image correlation method, Construct. Build. Mater. 147 (2017) 194–202.

[24] R. Aghlara, M.M. Tahir, Measurement of strain on concrete using an ordinary digital camera, Measurement 126 (2018) 398–404.

[25] Z. Huang, Y. Tu, S. Meng, C. Sabau, C. Popescu, G. Sas, Experimental study on shear deformation of reinforced concrete beams using digital image correlation, Eng. Struct. 181 (2019) 670–698.

[26] Y. Chen, J. Wei, H. Huang, W. Jin, Q. Yu, Application of 3D-DIC to characterize the effect of aggregate size and volume on non-uniform shrinkage strain distribution in concrete, Cement Concr. Compos. 86 (2018) 178–189.

[27] I. Maruyama, H. Sasano, M. Lin, Impact of aggregate properties on the development of shrinkage-induced cracking in concrete under restraint conditions, Cement Concr. Res. 85 (2016) 82–101.

[28] P. Goltermann, Mechanical predictions of concrete deterioration. Part 2: classification of crack patterns, ACI Mater. J. 92 (1995) 58–63.

[29] J.H. Moon, Shrinkage, Residual Stress, and Cracking in Heterogeneous Materials, PhD thesis, Purdue University, West Lafayette, Indiana, May 2006.

[30] GB T50081-2002, Standard for Test Method of Mechanical Properties on Ordinary Concrete, China Academy of Building Research, China, 2002.

[31] E. Schlangen, J.G.M. Van Mier, Simple lattice model for numerical simulation of fracture of concrete materials and structures, Mater. Struct. 25 (1992) 534–542.

[32] Z. Qian, E. Schlangen, G. Ye, K. Van Breugel, Prediction of mechanical properties of cement paste at microscale, Mater. Construcción 60 (2010) 7–18.

[33] H. Zhang, B. Šavija, S.C. Figueiredo, M. Lukovic, E. Schlangen, Microscale testing and modelling of cement paste as basis for multi-scale modelling, Materials 9 (2016) 907.

[34] H. Zhang, B. Šavija, S.C. Figueiredo, E. Schlangen, Experimentally validated multi-scale modelling scheme of deformation and fracture of cement paste, Cement Concr. Res. 102 (2017) 175–186.

[35] H. Zhang, Y. Xu, Y. Gan, Z. Chang, E. Schlangen, B. Šavija, Combined experimental and numerical study of uniaxial compression failure of hardened cement paste at micrometre length scale, Cement Concr. Res. 126 (2019) 105925.

[36] Z. Wu, H.S. Wong, N.R. Buenfeld, Influence of drying-induced microcracking and related size effects on mass transport properties of concrete, Cement Concr. Res. 68 (2015) 35–48.

[37] F.O. Slate, S. Olsefski, X-rays for study of internal structure and microcracking of concrete, J. Am. Concr. Inst. 60 (1963) 575–588.

[38] Z.C. Grasley, C.K. Leung, Desiccation shrinkage of cementitious materials as an aging, poroviscoelastic response, Cement Concr. Res. 41 (2011) 77–89.

[39] Z.P. Bažant, M. Jirásek, Creep and Hygrothermal Effects in Concrete Structures, Springer, Dordrech, The Netherlands, 2018.